Bifunctional Water Splitting Photoelectrocatalysts Using Flexible Organometallic Complex and Nanographene Multilayer Thin Films

Dongseok Kim,[†1] Minsu Gu,[†‡1] Yeongkyu Choi,[2] Hyunwoo Kim,[3,4] Jungki Ryu,[3,4] and Byeong-Su Kim[1]**

[1]Department of Chemistry, Yonsei University, Seoul 03722, Republic of Korea

[2]Department of Chemistry, [3]Department of Energy Engineering, and [4]Emergent Hydrogen Technology R&D Center, Ulsan National Institute of Science and Technology (UNIST), Ulsan 44919, Republic of Korea

[†]These authors contributed equally to this work.

[‡]Current address: Department of Chemistry, The University of Texas at Austin, Austin 78712, United States

E-mail: sbgms@yonsei.ac.kr (M.G.); bskim19@yonsei.ac.kr (B.-S.K.)

Table S1. Previous literatures for Ru complex based photoelectrochemical cells non-assisted by photocatalytic metal oxide.

Substrate	Active materials	Photoanodic current ($\mu A/cm^2$)	Anodic bias	Photocathodic current ($\mu A/cm^2$)	Cathodic bias	Electrolyte	Method	Ref.
ITO	Ru complex / nGO	4.28	0 V vs RHE	28.42	1.23 V vs RHE	Potassium phosphate buffer at pH 7	LbL assembly	This work
ITO	Ru complex EuBW	-	-	8.47	-0.3 V vs. SCE	0.2 M Na_2SO_4	LbL assembly	S1
ITO	Ru complex Phosphomolybdic acid	~7.5	vs. $Hg/HgCl_2$	-	-	50 mmol/L KCl	Langmuir blodgett	S2
ITO	Ru complex GO-PEG	-	-	2.8	-0.4 V vs. SCE	0.2 M Na_2SO_4	Drop casting	S3
ITO	Ru complex MWCNT, PVA	0.05	0.9 V vs. $Ag/AgNO_3$	-	-	0.1 M $TBAPF_6$ in acetonitrile	LbL assembly	S4
ITO	Ru complex AgNP	-	-	~0.045	-0.5 V vs. Ag/AgCl	0.1 M $TBAPF_6 \cdot CHCl_3$	Molecular immobilization	S5
ITO	Ru complex GO	-	-	7.43	-0.4 V vs. SCE	0.1 M Na_2SO_4	LbL assembly	S6
ITO	Ru complex	-	-	2.72	-0.4 V vs. SCE	0.1 M Na_2SO_4	Covalently self-assembly	S7
Pt flag	Ru complex POM	59	1.0 V vs. Ag/AgCl	-	-	1 mM $(Bu)_4NBF_4$	LbL assembly	S8

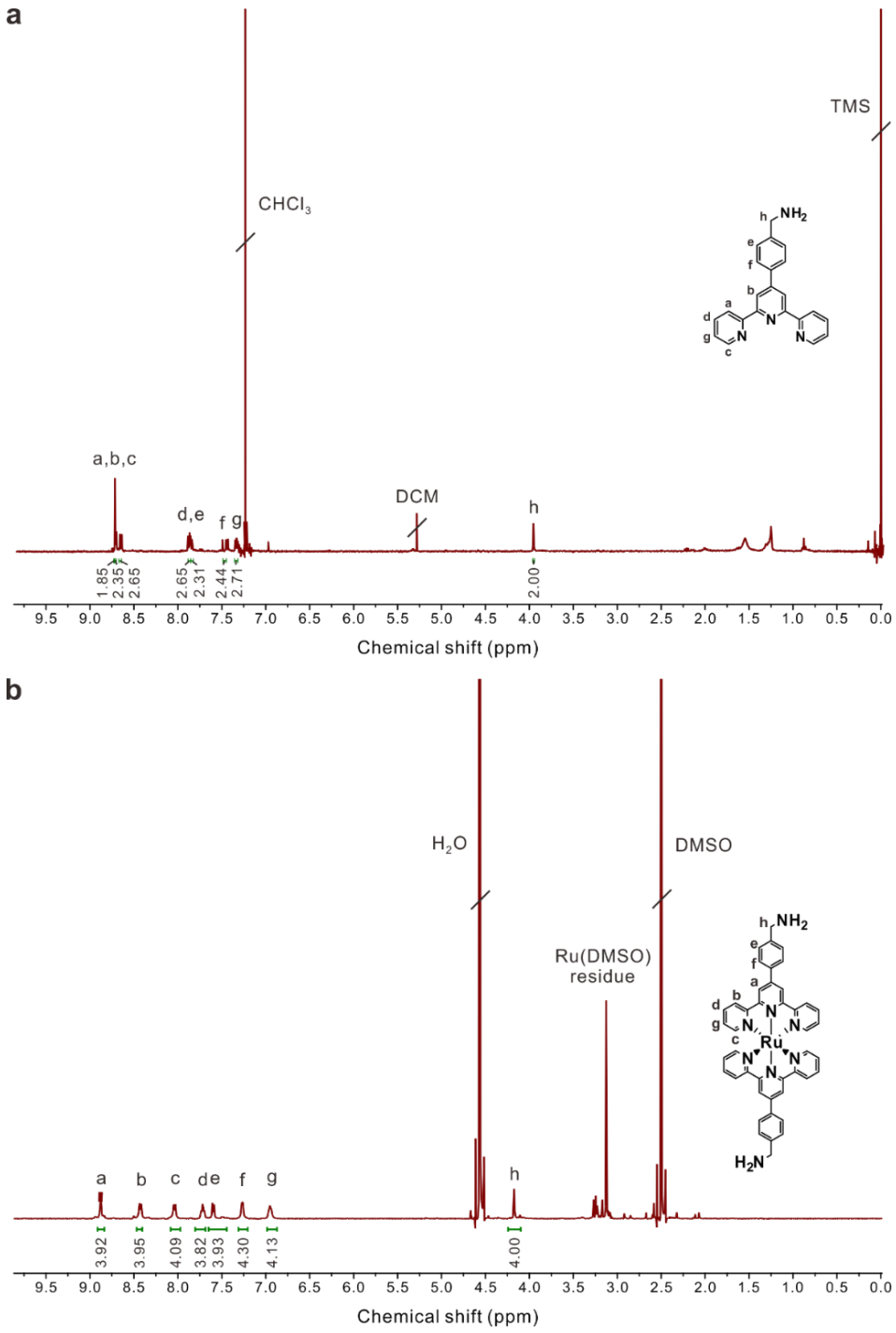

Figure S1. ^{1}H NMR spectra of (a) TPY ligand and (b) TPY_2Ru complex.

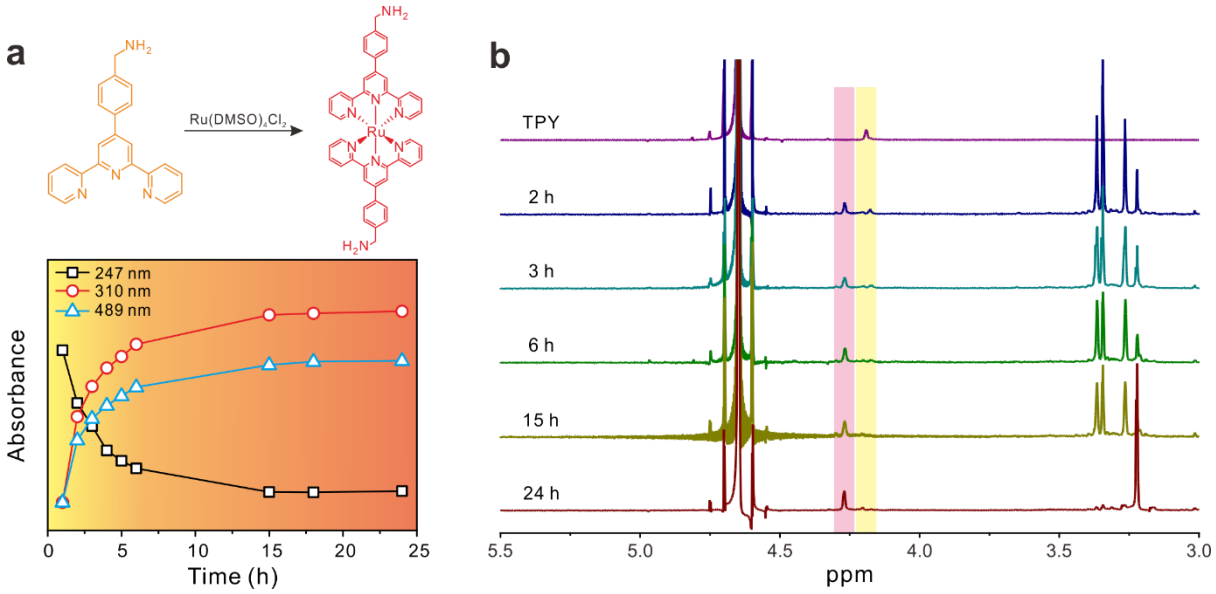

Figure S2. Progress of TPY_2Ru-complex formation. (a) Changes in UV/vis absorption peaks corresponding to π-π* transition of the TPY moiety at 247 nm, electron delocalization on the TPY moiety at 310 nm, and MLCT band of metal-ligand complex at 489 nm, respectively. (b) Deshielding effect of electron delocalization upon complexation observed through *ex-situ* ^1H NMR spectra of the formation of TPY_2Ru complex.

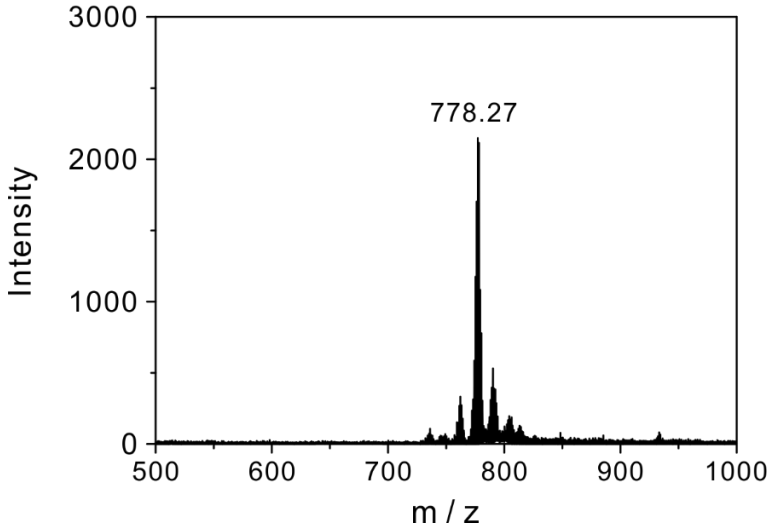

Figure S3. MALDI-TOF spectrum of TPY_2Ru complex ($C_{44}H_{36}N_8Ru$: 778.21).

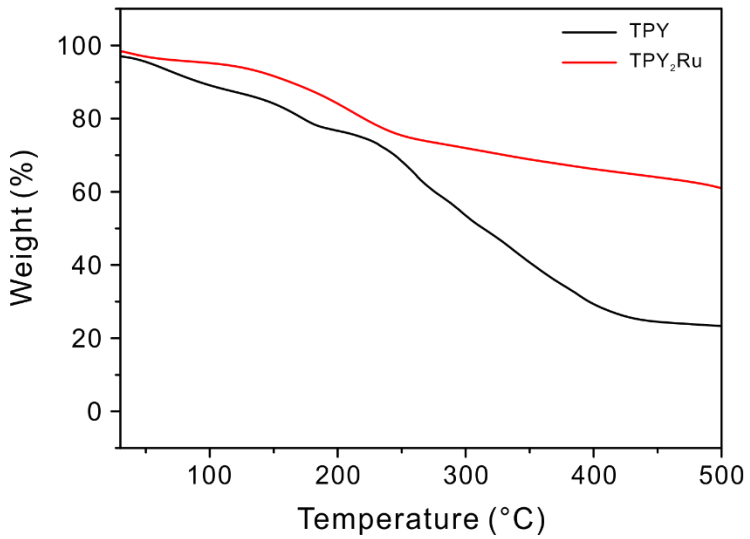

Figure S4. TGA results of the (black) TPY ligand and (red) TPY_2Ru complex at a heating rate of 5 °C per min in N_2 atmosphere.

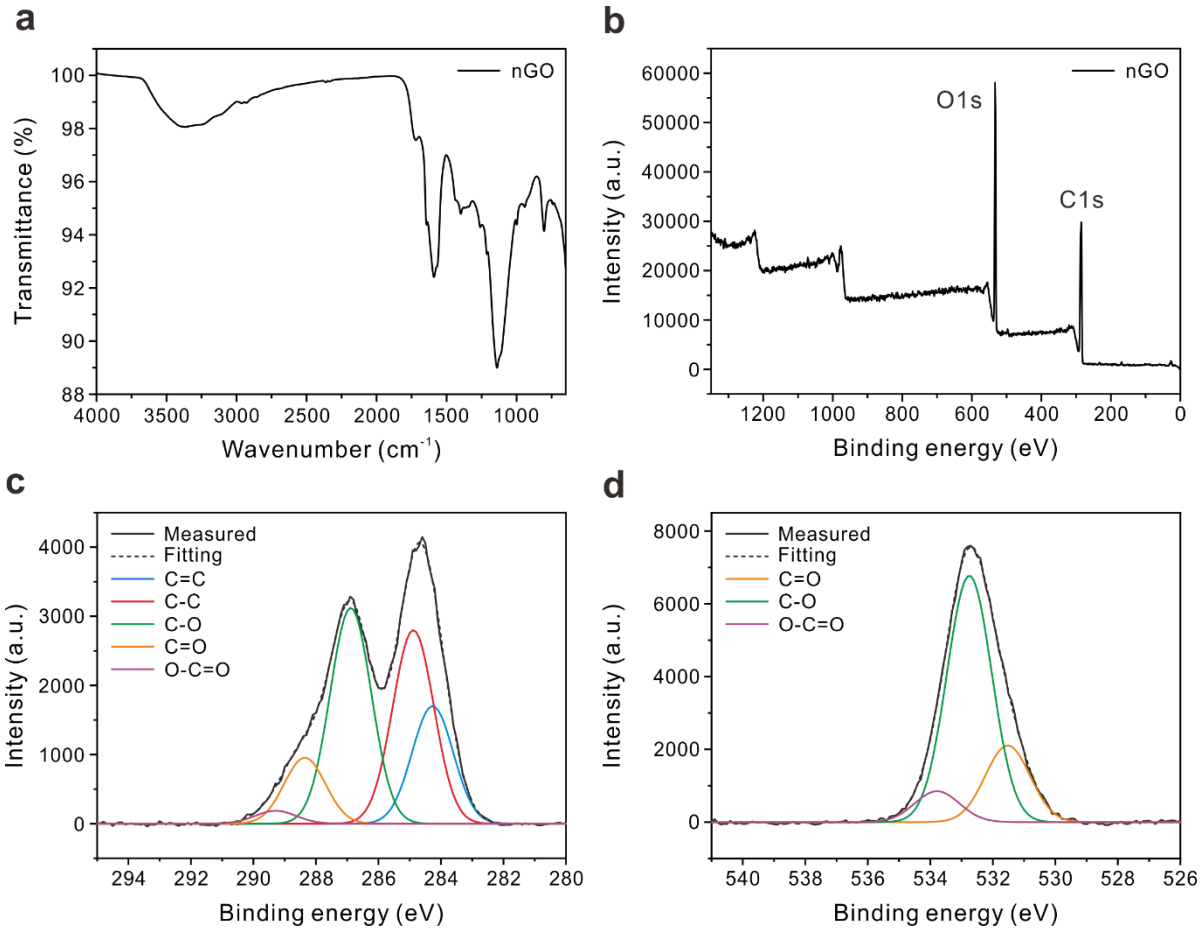

Figure S5. Characterizations of nGO with (a) FT-IR and (b-d) XPS spectroscopy. (b) Survey spectrum and (c, d) deconvoluted high-resolution XPS spectra of (c) C1s and (d) O1s of nGO.

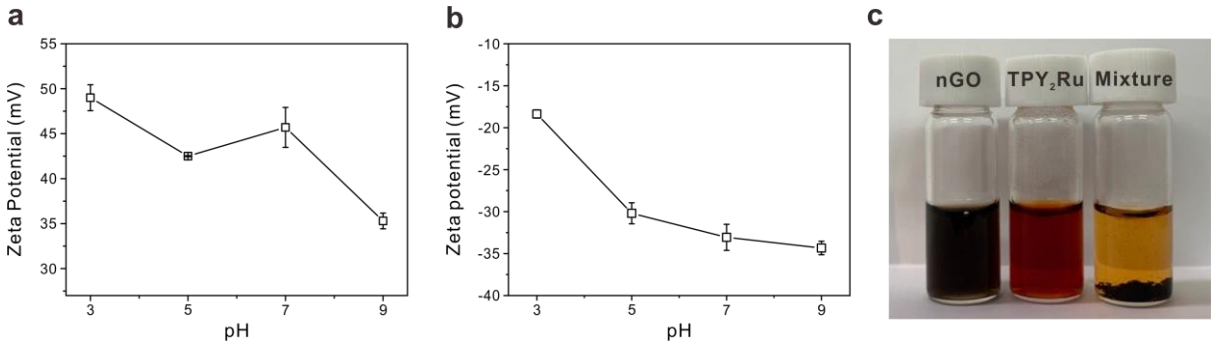

Figure S6. ζ-potential of the (a) TPY_2Ru complex and (b) nGO at various pH conditions. (c) Photographic images of aqueous dispersions of nGO, TPY_2Ru complex, and a simple mixture.

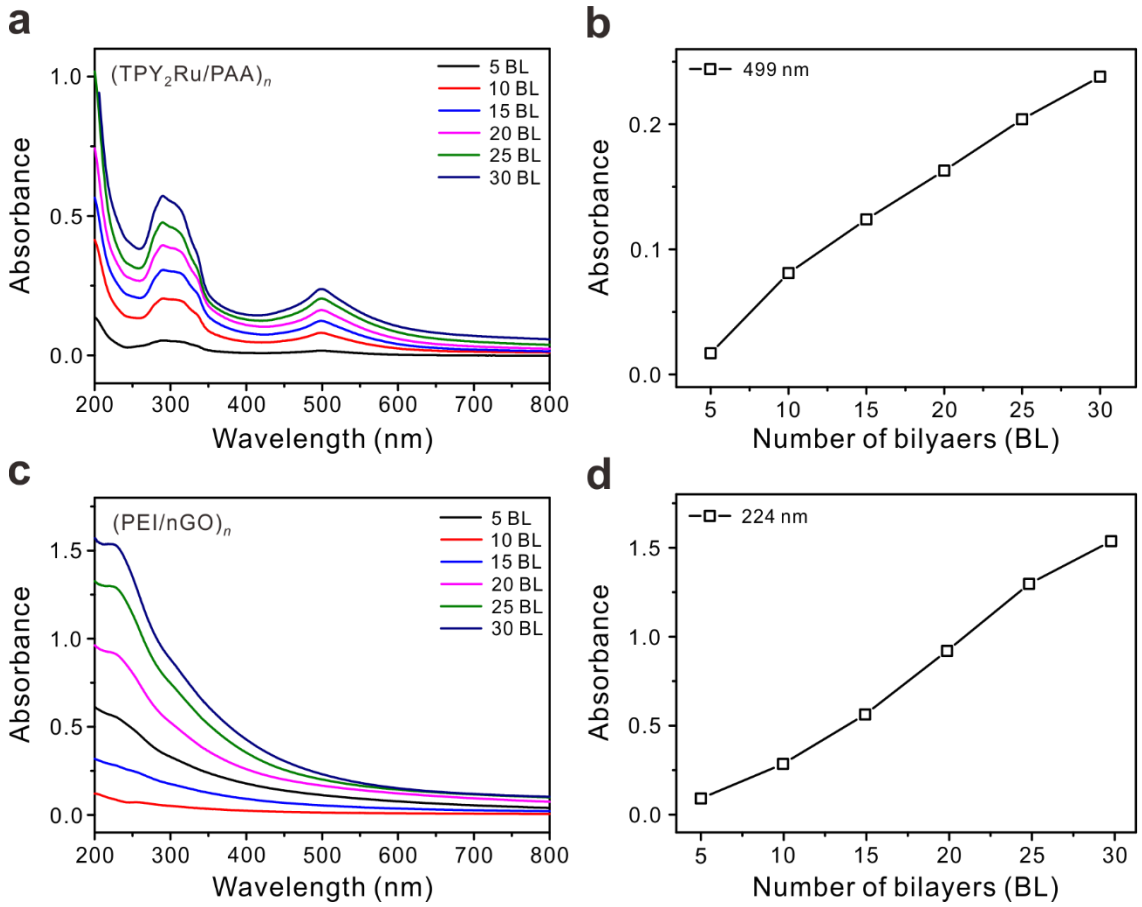

Figure S7. LbL growth curves of two control multilayer electrodes. (a) UV/vis absorbance spectra of $(TPY_2Ru/PAA)_n$ multilayer electrodes and (b) absorbance at 499 nm corresponding to the absorbance maxima of TPY complex. (c) UV/vis absorbance spectra of $(PEI/nGO)_n$ multilayer electrodes and (d) absorbance at 224 nm corresponding to the absorbance maxima of nGO.

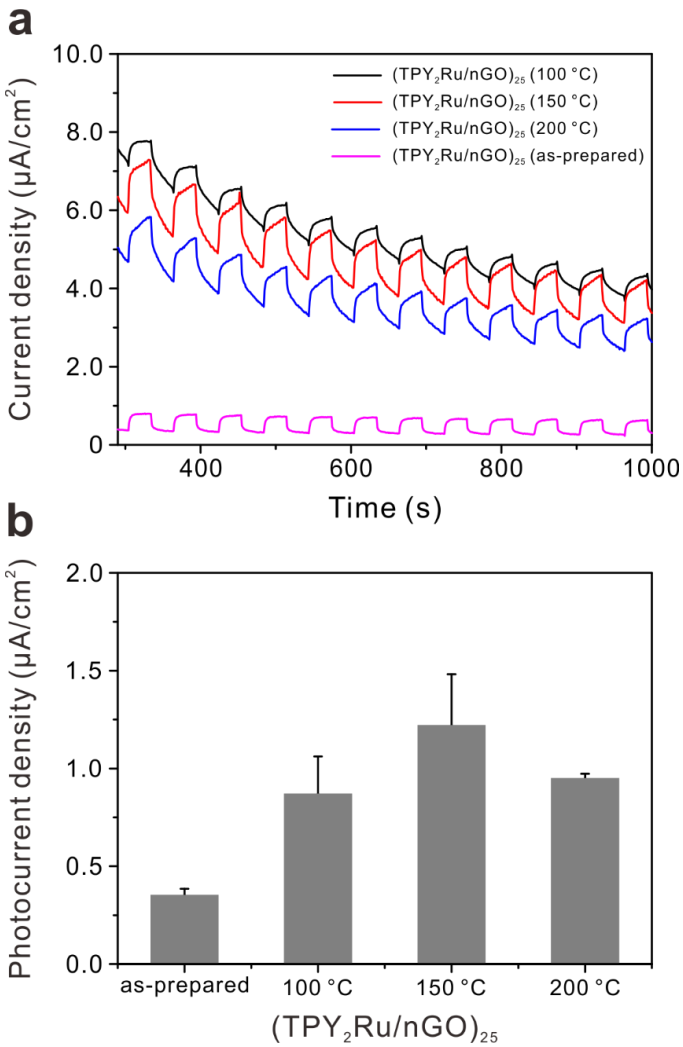

Figure S8. (a, b) PEC performance of the $(TPY_2Ru/nGO)_{25}$ multilayer film electrodes as a function of annealing temperature for optimizing reduction temperature of nGO. (a) Chronoamperometry and (b) on-off photocurrent density. Chronoamperometry was conducted in 0.10 M KCl solution at 0.62 V vs Ag/AgCl.

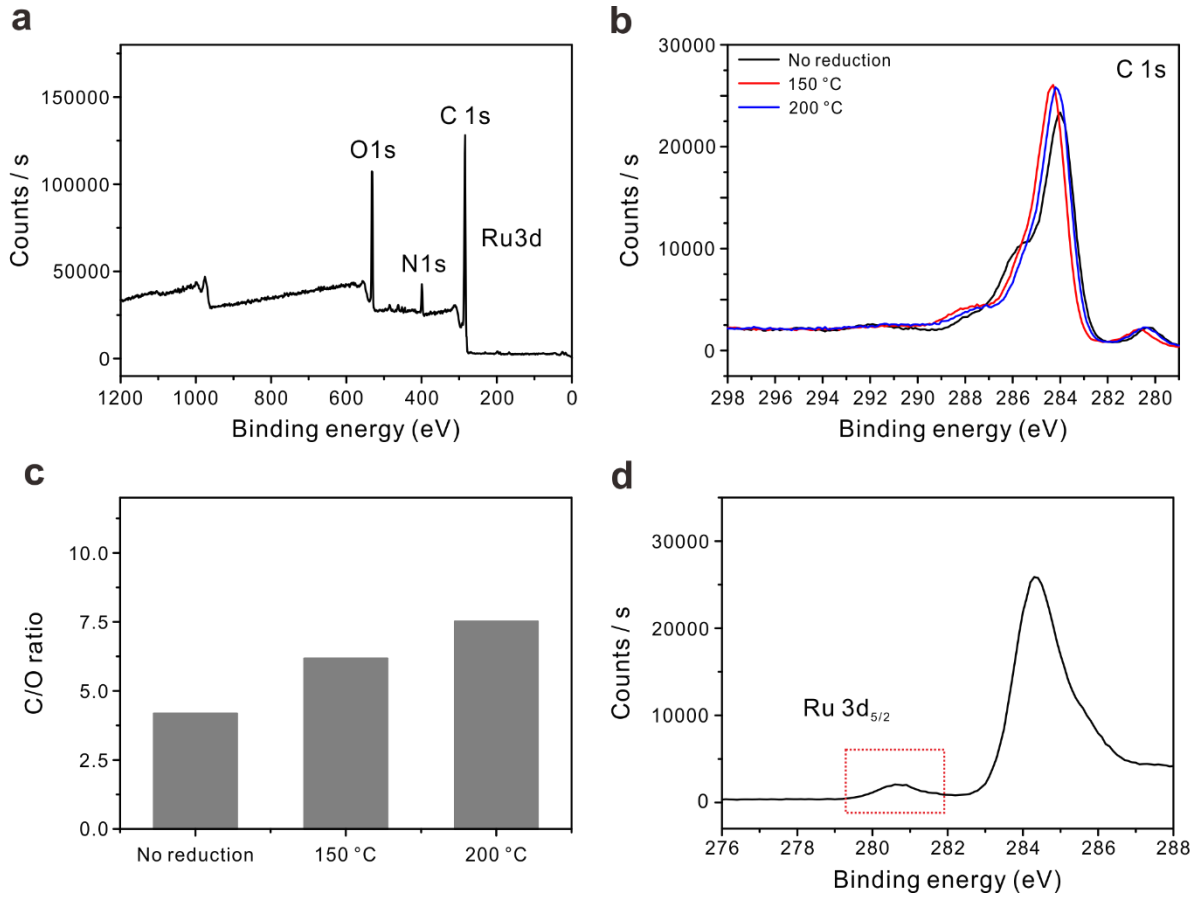

Figure S9. (a–d) Characterizations of $(TPY_2Ru/nGO)_{30}$ multilayer electrodes by XPS. (b) High-resolution C1s XPS spectra of $(TPY_2Ru/nGO)_{30}$ multilayer electrode treated at different reduction temperatures. (c) Changes in C/O ratio based on C1s XPS spectra, depending on the annealing temperature. (d) Ru 3d XPS spectra of $(TPY_2Ru/nGO)_{30}$ multilayer film electrode after a thermal reduction of 150 °C.

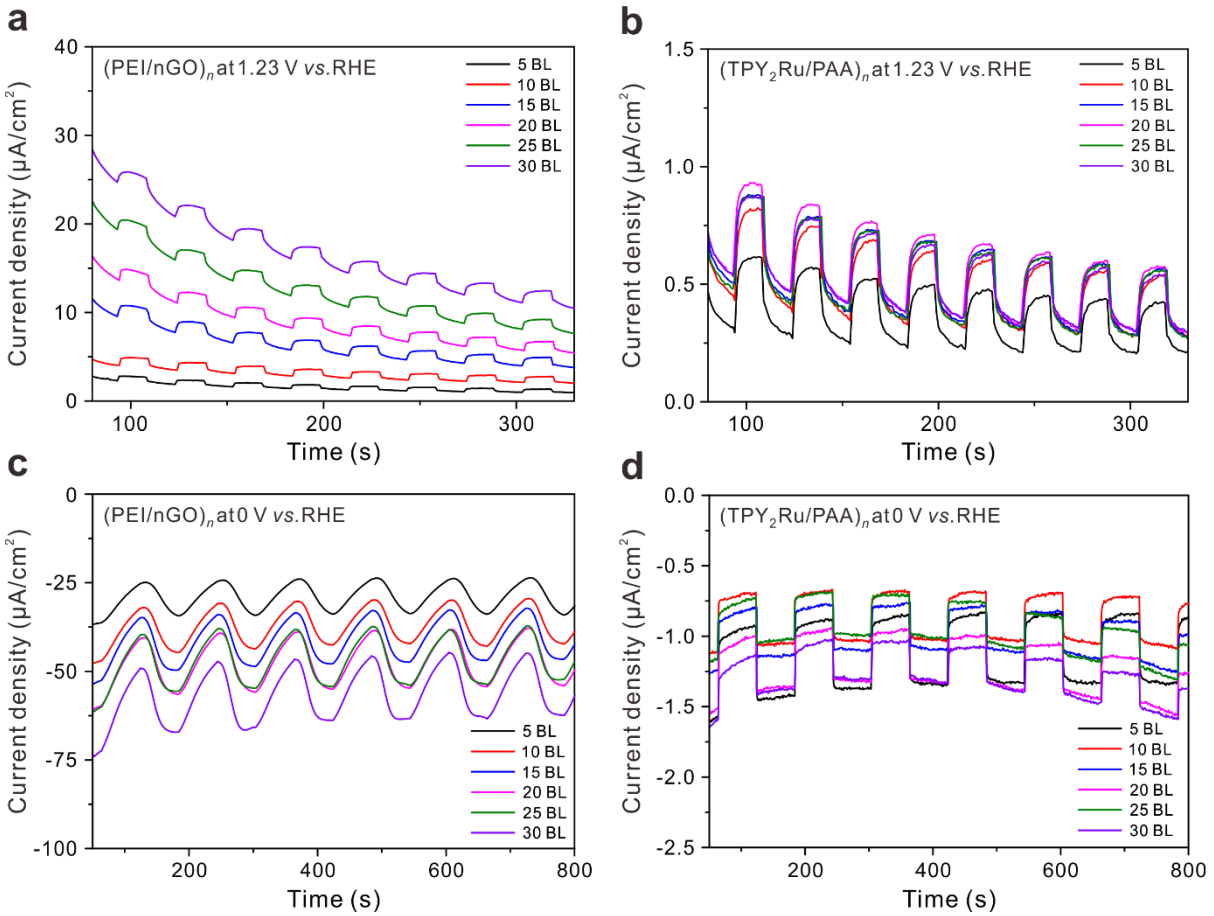

Figure S10. Chronoamperometry data of two control multilayer electrodes. (a, b) $(PEI/nGO)_n$ multilayer electrode for (a) OER and (b) HER. (c, d) $(TPY_2Ru/PAA)_n$ multilayer electrode for (c) OER and (d) HER as a function of the number of BLs. All experiments were conducted with intermittent visible light irradiation in the presence of 0.10 M potassium phosphate buffer at each redox potential for water splitting at pH 7.

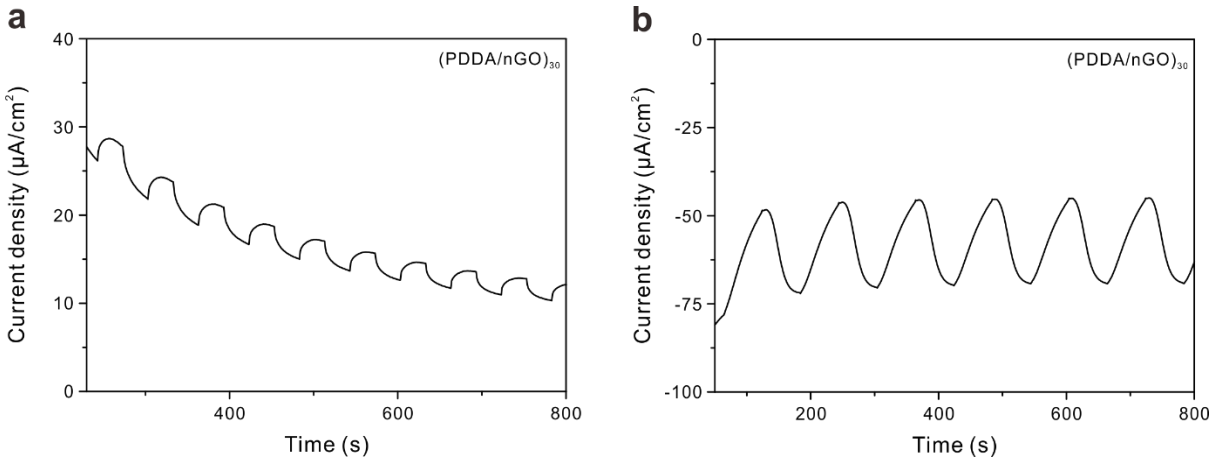

Figure S11. Chronoamperometry data of the $(PDDA/nGO)_{30}$ multilayer electrode for (a) OER and (b) HER with and without visible light irradiation in 0.10 M potassium phosphate buffer at each redox potential for water splitting at pH 7.

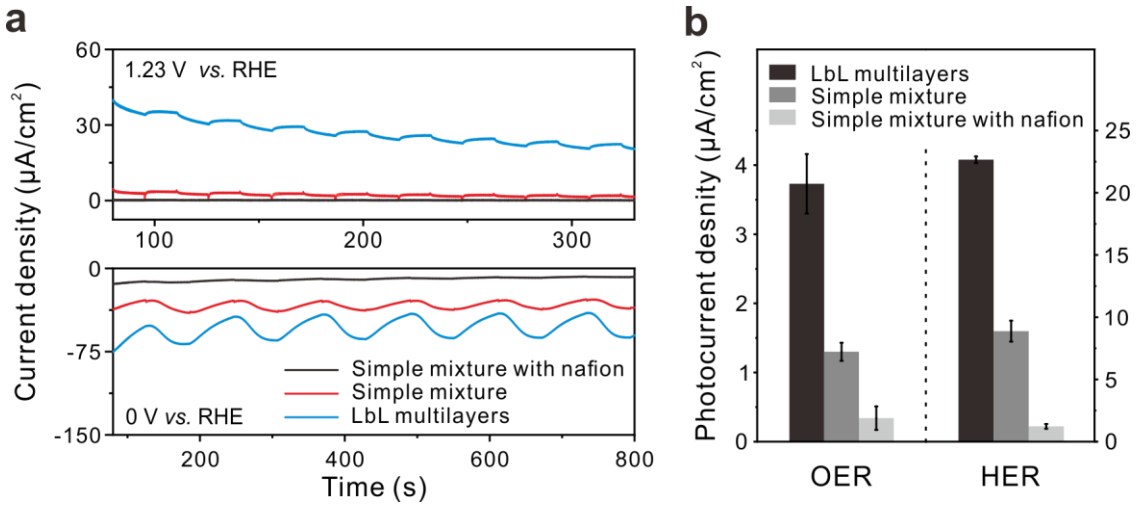

Figure S12. (a) Chronoamperometry data under intermittent light and (b) comparison of the photocurrent density between the $(TPY_2Ru/nGO)_{30}$ multilayer electrode and simple mixture of TPY_2Ru and nGO for respective OER and HER at each redox potential for water splitting measured in 0.10 M potassium phosphate buffer at pH 7. For preparation of a simple mixture sample, 100 μL of mixture suspension (200 μg/mL) with or without 50 μL of Nafion 117 (5 wt%) was drop-casted on the ITO electrodes.

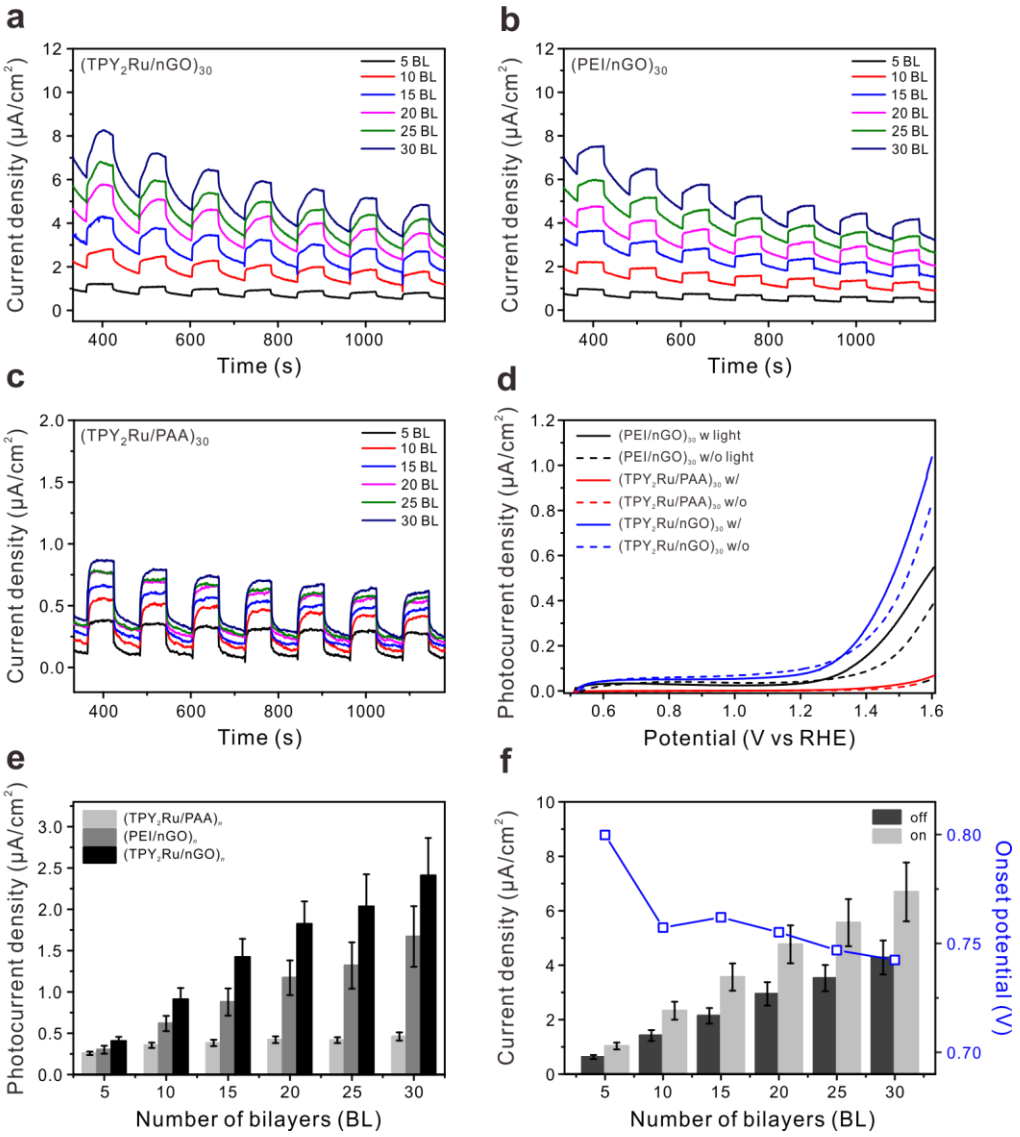

Figure S13. PEC performances of (a) $(TPY_2Ru/nGO)_n$, (b) $(PEI/nGO)_n$, and (c) $(TPY_2Ru/PAA)_n$ multilayer thin films in 0.10 M KCl electrolyte at 0.62 V vs Ag/AgCl. (d) Linear sweep voltammetry (LSV) data of each multilayer film electrode with visible light irradiation. (e) Comparison of photocurrent densities between different types of multilayer film electrodes for OER. (f) Current density of $(TPY_2Ru/nGO)_n$ photocatalytic multilayer film with and without visible light irradiation and onset potential for OER with respect to the number of BLs.

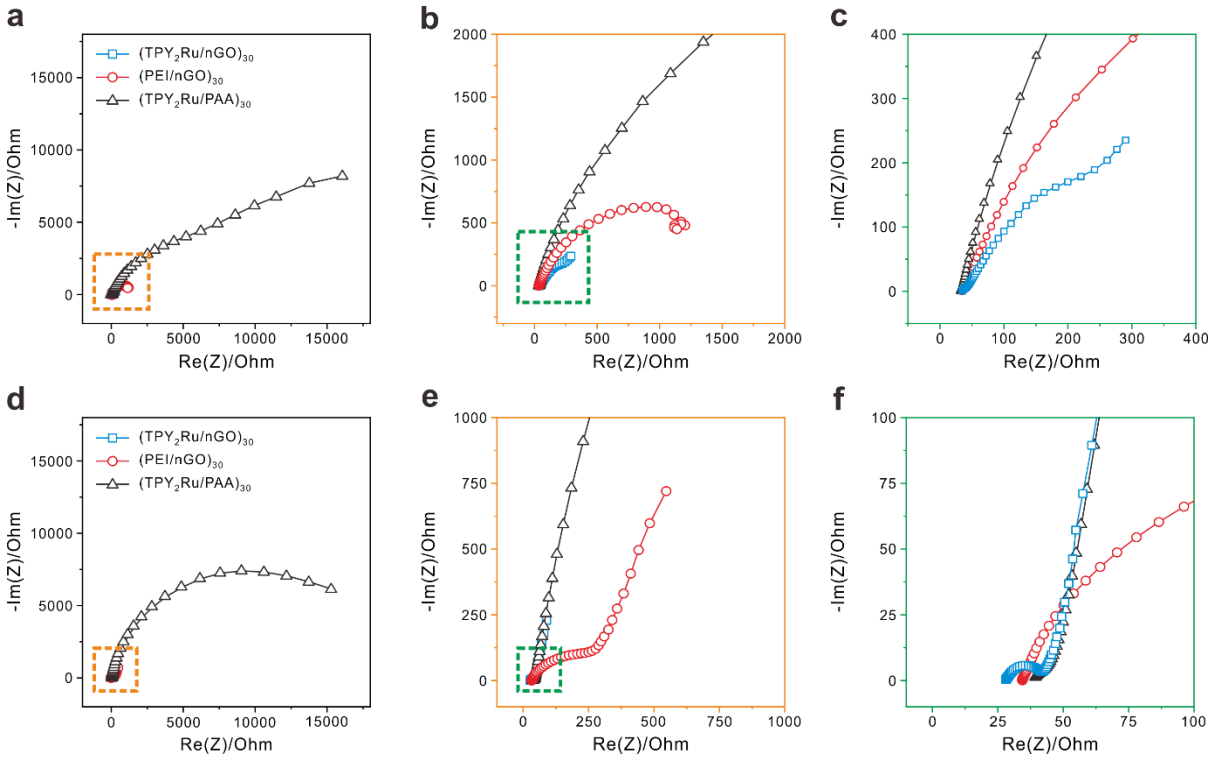

Figure S14. Nyquist plots of electrochemical impedance spectroscopy (EIS) for three different multilayer electrodes; (blue) $(TPY_2Ru/nGO)_{30}$, (red) $(PEI/nGO)_{30}$, and (black) $(TPY_2Ru/PAA)_{30}$ under visible light irradiation at (a) 1.41 V *vs.* RHE for photoanode and (d) 0 V *vs.* RHE for photocathode. (b), (c), (e) and (f) show enlarged graphs of all the boxes.

Table S2. A proposed two RC circuit models and fitting results of the Nyquist plot in Figure S13. R_s, R_{ct1}, and R_{ct2} indicate series resistance of the underlying substrate and solution, charge transport resistance in the photocatalytic multilayer electrodes, and charge transfer resistance of catalytic reaction at the photoelectrode/electrolyte interface, respectively. Warburg impedance (W_1) represents the mass transport in the multilayer electrodes.

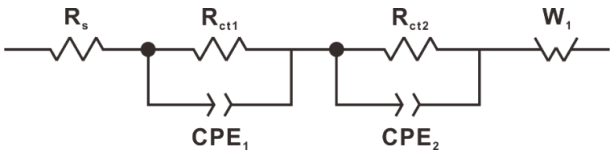

Fitting results of Nyquist plot in Figure S13 at 1.41 V *vs.* RHE for OER

Sample	R_s (Ω)	R_{ct1} (Ω) / CPE_1 (μF)	R_{ct2} (Ω) / CPE_2 (μF)	W_1 (Ω ·$s^{1/2}$)
$(TPY_2Ru/nGO)_{30}$	34.48	13.90 / 15.44	41.63 / 5157	198.2
$(PEI/nGO)_{30}$	33.21	66.49 / 103.10	769.5 / 112.5	427.5
$(TPY_2Ru/PAA)_{30}$	30.88	1595 / 26.2	10847 / 55.65	725

Fitting results of Nyquist plot in Figure S13 at 0 V *vs.* RHE for HER

Sample	R_s (Ω)	R_{ct1} (Ω) / CPE_1 (μF)	R_{ct2} (Ω) / CPE_2 (μF)	W_1 (Ω ·$s^{1/2}$)
$(TPY_2Ru/nGO)_{30}$	28.61	12.08 / 39.44	1520 / 8368	19.94
$(PEI/nGO)_{30}$	33.14	23.48 / 110.40	74.68 / 159.10	379.5
$(TPY_2Ru/PAA)_{30}$	39.5	1495 / 75.27	13895 / 43.9	568.9

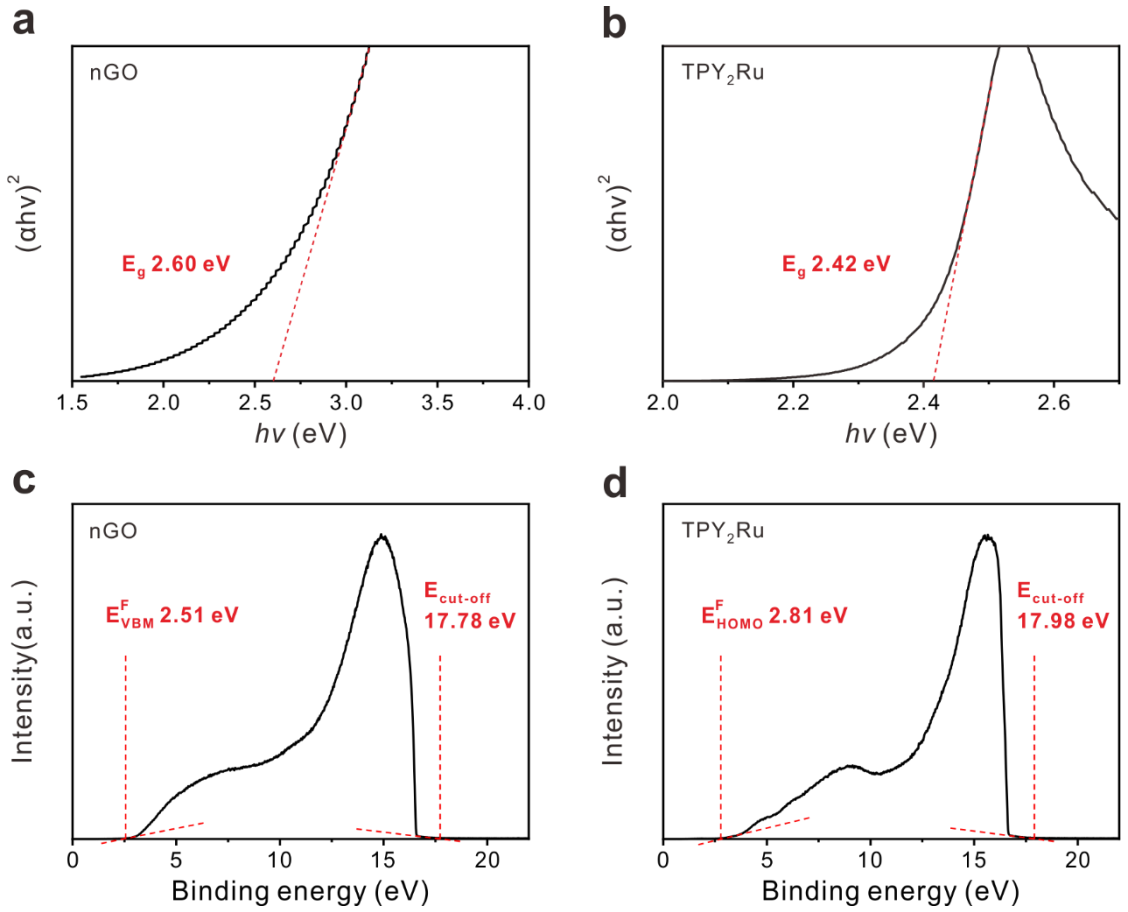

Figure S15. Band-gap energy of (a) nGO and (b) TPY_2Ru from UV/vis absorption using the Tauc plot method. Ultraviolet photoelectron spectroscopy (UPS) spectra for the (c) nGO and (d) TPY_2Ru complex. The valence band maximum (VBM) and HOMO level were determined by the intercepts of the tangent line at the low binding energy, following the previously reported method.[S9] The cut-off energy of the secondary electron was determined by the intercept of the tangent line at the high binding energy. The ionization potential was calculated by subtracting the width of UPS spectra.

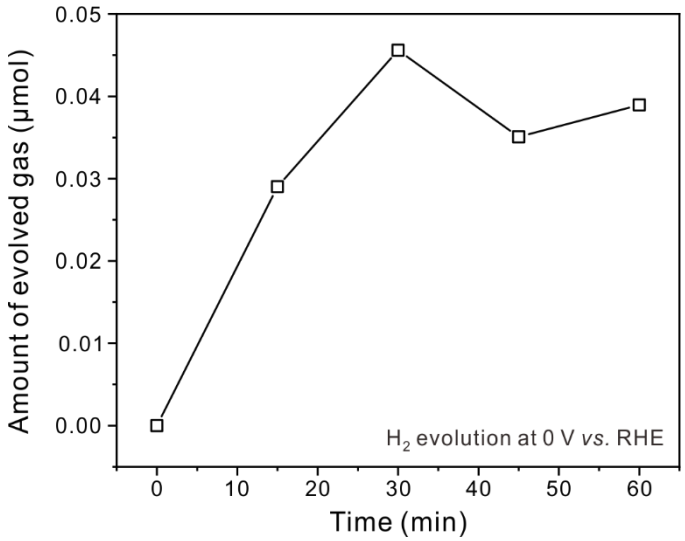

Figure S16. Gas chromatography-based gas evolution by the $(TPY_2Ru/nGO)_{30}$ photoelectrode in half-cell operated at 0 V vs. RHE for HER without any cocatalyst.

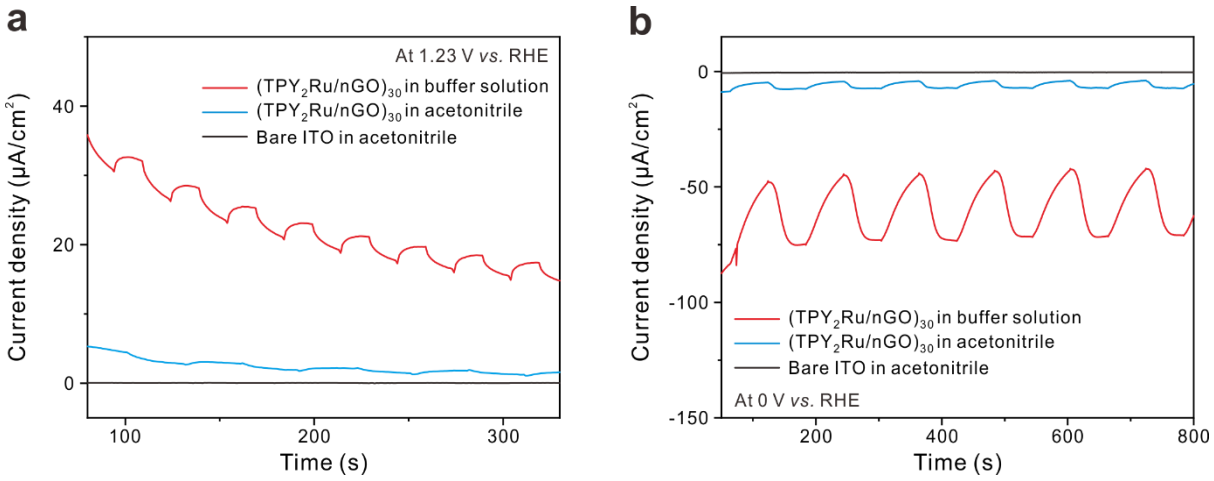

Figure S17. Comparison of current density for $(TPY_2Ru/nGO)_{30}$ photoelectrodes measured in 0.10 M potassium phosphate buffer and acetonitrile containing 0.10 M tetrabutylammonium hexafluorophosphate ($TBAPF_6$) at (a) 1.23 V *vs.* RHE and (b) 0 V *vs.* RHE.

REFERENCES

(S1) Ye, H. Y.; Qi, J. M.; Sun, R.; Gao, L. H.; Wang, K. Z., Photoelectric Active Hybrid Film Based on Ru^{II} Terpyridyl Complex and Eu^{III} Substituted Keggin Polyoxometalate of $[Eu(BW_{11}O_{39})]_2^{15-}$. *Electrochim. Acta* **2017,** *256*, 291-298.

(S2) He, W. L.; Chen, J. L.; Chen, M.; Qian, D. J., Interfacial Self-Assembly, Characterization, Electrochemical, and Photo-catalytic Properties of Porphyrin-Ruthenium Complex/ Polyoxomelate Triad Hybrid Multilayers. *Colloids Surf. A* **2016,** *509*, 1-10.

(S3) Huang, J.; Wang, D. D.; Yue, Z. K.; Li, X.; Chu, D. M.; Yang, P., Ruthenium Dye N749 Covalently Functionalized Reduced Graphene Oxide: A Novel Photocatalyst for Visible Light H_2 Evolution. *J. Phys. Chem. C* **2015,** *119* (50), 27892-27899.

(S4) Jeong, D. C.; Song, S. G.; Satheeshkumar, C.; Lee, Y.; Kim, K. S.; Song, C., Enhanced Photoinduced Electron Transfer by Multiwalled Carbon Nanotubes in Self-Assembled Terpyridine Polymer Networks. *Polymer* **2015,** *69*, 39-44.

(S5) Kajikawa, A.; Togashi, T.; Orikasa, Y.; Cui, B. B.; Zhong, Y. W.; Sakamoto, M.; Kurihara, M.; Kanaizuka, K., Construction of Hybrid Films of Silver Nanoparticles and Polypyridine Ruthenium Complexes on Substrates. *Dalton Trans.* **2015,** *44* (34), 15244-15249.

(S6) Yang, W.; Zheng, Z. B.; Meng, T. T.; Wang, K. Z., Synergistically Enhanced Photoelectrochemical Properties of a Layer-by-Layer Hybrid Film Based on Graphene Oxide and a Free Terpyridyl-Grafted Ruthenium Complex. *J. Mater. Chem. A* **2015,** *3* (7), 3441-3449.

(S7) Lin, H.; Dai, Y. C.; Chen, X.; Huang, Q. Y.; Wang, K. Z., Preparation and Electrochemical and Photoelectrochemical Properties of a Covalently Self-Assembled Monolayer Film Based on a Bis-terpyridyl ruthenium(II) Complex. *Thin Solid Films* **2013,** *542*, 251-256.

(S8) Walsh, J. J.; Zhu, J.; Bond, A. M.; Forster, R. J.; Keyes, T. E., Visible Light Sensitized Photocurrent Generation from Electrostatically Assembled Thin Films of $Ru(bpy)_3^{2+}$ and The Polyoxometalate Gamma*- $W_{18}O_{54}(SO_4)_2^{4-}$: Optimizing Performance in a Low Electrolyte Medium. *J. Electroanal. Chem.* **2013,** *706*, 93-101.

(S9) Nguyen, B.-S.; Xiao, Y.-K.; Shih, C.-Y.; Nguyen, V. -C.; Chou, W.-Y.; Teng, H., Electronic Structure Manipulation of Graphene Dots for Effective Hydrogen Evolution from Photocatalytic Water Decomposition. *Nanoscale* **2018**, *10* (22), 10721-10730.